Adaptive reconstruction of radar reflectivity in clutter-contaminated areas by accounting for the space-time variability

Shinju Park* and Marc Berenguer

Centre de Recerca Aplicada en Hidrometeorologia, Universitat Politècnica de Catalunya, Barcelona, Spain

(*) Currently at Center for Atmospheric REmote sensing (CARE), Kyungpook National University, Daegu, South Korea.

Corresponding author: Shinju Park, Centre de Recerca Aplicada en Hidrometeorologia, Universitat Politècnica de Catalunya, E08034 Barcelona, Spain (shinju.park@gmail.com).

Abstract

Identification and elimination of clutter is necessary for ensuring data quality in radar Quantitative Precipitation Estimates (QPE). For uncorrected scanning reflectivity after signal processing, the removed areas have been often reconstructed by horizontal interpolation, extrapolation of non-contaminated PPIs aloft, or combining both based on a classification of the precipitation type. We present a general reconstruction method based on the interpolation of clutter-free observations. The method adapts to the type of precipitation by considering the spatial and temporal variability of the field provided by the multi-dimensional semivariogram. Six different formulations have been tested to analyze the gain introduced by each source of information: (1) horizontal interpolation, (2) vertical extrapolation, (3) extrapolation of past observations, (4) volumetric reconstruction, (5) horizontal and temporal reconstruction, and (6) volumetric and temporal reconstruction. The evaluation of the reconstructed fields obtained with the 6 formulations has been done (i) over clutter-free areas by comparison with the originally observed values, and (ii) over the real clutter-contaminated areas by comparison with the rainfall accumulations from a raingauge network. The results for 24 analyzed events (with a variety of convective and widespread cases) suggest that the contribution of extrapolation of past observations is not fundamental, and that the volumetric reconstruction is the one that overall adapted the best to the different situations.

1 Introduction

The production of radar Quantitative Precipitation Estimates (QPE) requires processing the observations to ensure their quality and its conversion into the variable of interest (e.g., precipitation rates near the surface). This processing is done through a chain of algorithms applied to mitigate the sources of uncertainty that affect radar observations: radar miscalibration, beam blockage, ground and sea clutter associated with anomalous propagation, path and radome attenuation, the vertical variability of precipitation combined with the loss of representativeness of radar observations with range, or the variability of the drop size distribution that controls the conversion of the measured variables into precipitation rate [e.g., Corral et al. (2009); Villarini and Krajewski (2009)].

Some of these algorithms involve the reconstruction of the meteorological signal in areas where the signal is lost (e.g., due to total beam blockage, severe path attenuation by heavy rain) or strongly contaminated, for instance, in the areas affected by ground or sea clutter.

Identification and reconstruction of clutter-affected areas is often part of the signal processing through the analysis of the Doppler spectrum [e.g., Doviak and Zrnic (1993)]. However, this approach is known to have some limitations (i) to distinguish precipitation from clutter in the areas with Doppler velocities near zero, and (ii) to reconstruct the precipitation signal. As a result this processing causes, in many cases systematic underestimation of precipitation [e.g., Hubbert et al. (2009); Moiseev and Chandrasekar (2009)].

Alternatively, other clutter elimination approaches are applied to the uncorrected moment data (typically, reflectivity). This requires first identifying clutter areas, through the analysis of statistical properties of radar measurements based on decision trees or fuzzy logic concepts [e.g., Steiner and Smith (2002); Berenguer et al. (2006); Gourley et al. (2007) and references therein]. Secondly, the reconstruction of the meteorological signal is done by either horizontal

58 interpolation or extrapolation from the non-contaminated PPIs aloft [e.g., Bellon et al. (2007)
59 and Germann et al. (2006)]. A combination of the two was also proposed by Sánchez-Diezma
60 et al. (2001) by adapting the reconstruction to the type of precipitation affecting clutter-
61 contaminated areas: horizontal interpolation is used in widespread precipitation areas, and
62 vertical extrapolation is preferred for convective cells with some vertical development. In this
63 way, this method reduces the negative effects of strong gradients of the reflectivity field; i.e.,
64 widespread precipitation shows more variability in the vertical (specially related to the
65 presence of the bright band and the weaker reflectivity of solid precipitation), while
66 convective situations are typically characterized by high variability in the horizontal.
67 Hereafter, we will refer to this method as SSDZ2001.

68 In this paper, we propose a new reconstruction method that avoids the pre-classification used
69 by SSDZ2001 to choose between horizontal interpolation and vertical extrapolation. Instead,
70 the proposed method uses the available observations (in the horizontal, in the vertical and
71 from previous time steps) that are weighted based on the analysis of the spatial and temporal
72 structure of the rainfall field. Section 2 presents the different formulations of the method,
73 which has been used to reconstruct reflectivity fields in clutter-contaminated areas under
74 different rainfall situations (see Section 3). Evaluation of the results is presented in Section 4.

75 **2 Reconstruction method**

76 Once clutter echoes are removed from radar reflectivity measurements, it is necessary to fill
77 the resulting gaps with an estimate of the weather-related reflectivity. The reconstruction
78 method proposed here capitalizes on the spatial and temporal structure of the reflectivity field
79 [e.g., Zawadzki (1973)]. This section introduces first the general formulation of the proposed
80 method and, secondly, the specific formulations adapted to the use of different observations in
81 space and time.

2.1 General formulation

The reconstructed radar field at a location and time $\mathbf{x}=[x_o,y_o,z_o,t_o]$ is estimated as a linear combination of n clutter-free observations $Z(\mathbf{x}_i)$:

$$\hat{Z}(\mathbf{x}) = \sum_{i=1}^{n} \lambda_i \, Z(\mathbf{x}_i) \tag{1}$$

where λ_i is the weight given to the observation $Z(\mathbf{x}_i)$.

According to the Ordinary Kriging approach [e.g., Goovaerts (1997)], the optimal and unbiased estimate $\hat{Z}(\mathbf{x})$ can be obtained with the weights that are the solution of the following linear system:

$$\begin{bmatrix} \gamma_{11} & \cdots & \gamma_{1n} & 1 \\ \vdots & \ddots & \vdots & \vdots \\ \gamma_{n1} & \cdots & \gamma_{nn} & 1 \\ 1 & \cdots & 1 & 0 \end{bmatrix} \begin{bmatrix} \lambda_1 \\ \vdots \\ \lambda_n \\ \xi \end{bmatrix} = \begin{bmatrix} \gamma_1 \\ \vdots \\ \gamma_n \\ 1 \end{bmatrix}, \tag{2}$$

where γ_{ij} is the semivariogram for a separation vector $\mathbf{\Delta_{ij}}=\mathbf{x_i}-\mathbf{x_j}$, and γ_i is the one for a separation vector $\mathbf{\Delta_i}=\mathbf{x_i}-\mathbf{x}$. A Lagrange multiplier (ξ) is introduced to guarantee that the estimate $\hat{Z}(\mathbf{x})$ is unbiased. The semivariogram is a measure of the field variability and is generally defined as:

$$\gamma(\Delta) = \frac{1}{2}\mathrm{var}\left[Z(\mathbf{x}) - Z(\mathbf{x}+\Delta)\right] \approx \frac{1}{2}\frac{1}{N(\Delta)}\sum_{k=1}^{N(\Delta)}\left[Z(\mathbf{x}_k) - Z(\mathbf{x}_k+\Delta)\right]^2 \tag{3}$$

where Var[ ] denotes the variance operator, Δ is the lag in space and time, and $N(\Delta)$ is the number of points used to estimate the semivariogram for a separation Δ. Based on (3), further details on how the semivariograms have been estimated are presented in Appendix A.

2.2 Implemented reconstruction method

The general method presented above has been implemented to reconstruct the reflectivity gaps using 4-Dimensional neighboring clutter-free observations ($Z(\mathbf{x_i})$ in (1)): (i) within the PPI, (ii) in the closest non-contaminated PPI above, and (iii) the most recent radar volume scan (after compensating the effect of the motion). To illustrate the contribution of each of these components, the method has been configured as 3 formulations that use them separately (single-source formulations), and 3 other formulations that combine them.

2.2.1 Single-source formulations

2.2.1.1 HOR: Horizontal interpolation

The reflectivity estimate $\hat{Z}(\mathbf{x})$ at a given location and time $\mathbf{x}=[x_o,y_o,z_o,t_o]$ is reconstructed by interpolating the N_H neighboring non-contaminated observations on the same PPI and at the same time. That is, in (1), $Z(\mathbf{x_i})=Z(x_i,y_i,z_o,t_o)$. In our case, we use the N_H neighboring non-contaminated observations within the band of pixels surrounding the areas to be reconstructed [as is usually done by the methods based on horizontal interpolation, e.g., Bellon et al. (2007)]. Consequently, the number of points used in this reconstruction method, N_H, depends on the size and shape of the clutter area to be reconstructed.

2.2.1.2 VERT: Vertical extrapolation

The reflectivity estimate $\hat{Z}(\mathbf{x})$ at a given location and time $\mathbf{x}=[x_o,y_o,z_o,t_o]$ is obtained by extrapolating the closest non-contaminated reflectivity observation in the vertical. Note that

the reconstruction performed in this way does not apply the Ordinary Kriging approach, because the estimate is obtained by direct vertical extrapolation of a single observation; i.e., $\hat{Z}(x_o,y_o,z_o,t_o) = Z(x_o,y_o,z_i,t_o)$, where z_i represents the height of the closest clutter-free PPI.

2.2.1.3 NOW: Extrapolation of past observations with the motion field

The reconstructed value is taken as the observation in the previous Quality-Controlled volume scan taking into account the effect of the motion of precipitation. The estimate at a given location and time $\mathbf{x}=[x_o,y_o,z_o,t_o]$ is obtained by following its trajectory backwards in time with a semi-Lagrangian scheme: $\hat{Z}(x_o,y_o,z_o,t_o) = Z(x_o-u\cdot\Delta t,y_o-v\cdot\Delta t,z_o,t_o-\Delta t)$, where (u,v) stands for the motion field of Z, and Δt is the time between two consecutive scans. Similarly as for the VERT method, this approach does not apply the Ordinary Krigring approach because the reconstruction is done by direct extrapolation in time.

This procedure is very similar to what is done in nowcasting algorithms to extrapolate reflectivity observations to the future. The tracking algorithm to estimate the motion field and the extrapolation technique used here are the same as those presented by Berenguer et al. (2011).

2.2.2 Multiple-source formulations

The combination of the observations used in the three methods of section 2.2.1 is explored here. The novelty of the formulations presented below is that they allow an adaptive combination of the different sources of information in the Ordinary Kriging framework. The structure of the field as depicted by the semivariogram determines the weight given to each observation in (1) through the linear system of (2).

2.2.2.1 HV: Volumetric reconstruction

This formulation combines the observations used in methods HOR and VERT. Consequently, $n=N_H+1$ observations are used in equations (1) and (2) for the reconstruction of $\hat{Z}(x_o,y_o,z_o,t_o)$: (i) N_H neighboring observations on the same PPI, $Z(\mathbf{x_i})=Z(x_i,y_i,z_o,t_o)$, and (ii) one observation in the vertical extrapolated from the closest non-contaminated PPI above, $Z(\mathbf{x_i})=Z(x_o,y_o,z_i,t_o)$

2.2.2.2 HN: Horizontal-temporal reconstruction

This formulation combines the observations used in methods HOR and NOW.

2.2.2.3 HVN: Volumetric-temporal reconstruction

This formulation combines the observations used in methods HOR, VERT and NOW.

3 Data and study domain

The analysis domain is the area covered by the Corbera de Llobregat single-polarization C-band Doppler radar, located near Barcelona, northeast of Spain (white diamond in Fig. 1). The region has torrential characteristics, and a good part of the yearly rainfall totals (ranging from 400 to 1000 mm) are frequently accumulated during a few events along the year.

The evaluation of the proposed method has been done over 24 rainfall events occurred between 2001 and 2005 (see details in Table 1). The radar data were collected at a frequency of 5620 MHz and with a beam width of 0.90º and up to 240 km in range. Every 10 minutes the radar scans 20 PPIs for elevations between 0.5º and 25º, with a resolution of 2 km in range and 0.86º in azimuth. As part of the processing of radar reflectivity data, we have applied the algorithm of Delrieu et al. (1995) to mitigate the effect of beam blockage by the terrain. Non-

157 meteorological echoes have been identified with the technique of Berenguer et al. (2006). It is
158 based on a fuzzy-logic classifier that discriminates non-meteorological echoes from weather
159 echoes using a number of statistical features that characterize the properties of ground and sea
160 clutter. Finally, the reflectivity in clutter-contaminated areas has been reconstructed with the
161 method presented in Section 2.

162 Also, the rainfall records obtained with the raingauges available over the area (see Fig. 1)
163 have been used as reference in the evaluation.

164 **4 Evaluation**

165 We have applied the six formulations presented in section 2.2 to reconstruct clutter-
166 contaminated reflectivity over the volume scans collected for the 24 rainfall events of Table 1.

167 The evaluation of their performance requires a reference. However, a direct reference is not
168 available in the areas where the reflectivity field is contaminated by clutter. Here, we have
169 assessed the quality of the reconstructed estimates: (i) by implementing the techniques over a
170 clutter-free area where the originally observed values can be used as reference, and (ii) by
171 comparing radar rainfall estimates with the observations of a raingauge network over the real
172 clutter-contaminated areas.

173 Also, the performance of the proposed method has been compared with that of the technique
174 by SSDZ2001 (see section 1), which is currently implemented in the operational radar QPE
175 chain EHIMI (Corral et al., 2009).

176 **4.1 Reconstruction over clutter-free areas**

177 We have evaluated the reconstructed values by comparison with real radar observations over
178 clutter-free areas [similarly as done by Sánchez-Diezma et al. (2001)]. Figure 1 shows the

observed clutter map in mean propagation conditions and the clutter-free areas where this analysis has been performed (violet shading). The latter has been chosen to have the same structure as the observed clutter map, but has been rotated to guarantee that the reference value is available (i.e., the original data in these locations are not contaminated by clutter). The evaluation has been done in terms of event rainfall accumulations. These have been obtained using a Marshall and Palmer (1948) Z-R relationship. Note that using this Z-R is a simplification aiming at analyzing the results of the clutter reconstruction in rainfall units [i.e., the impact of the Z-R variability and its relationship with the type of precipitation are neglected (e.g., Sempere-Torres et al., 1998)].

The results are first illustrated for two characteristic events (a typical widespread situation and a strong convective case, respectively events #20 and #21 in Table 1), and then summarized for the rest of the cases.

4.1.1 Widespread case: 11 May 2004

On 11 May 2004, a widespread rainfall system affected the radar domain for about 24 hours and produced a rather uniform accumulation field (indicated by the low coefficient of variation) with a maximum raingauge value of 21.6 mm (see Table 1 and Fig. 2 left).

Table 2 shows the scores computed for the accumulations estimated from the reflectivity fields reconstructed with the different formulations of the proposed method. For this event, the best scores are obtained with the formulations that include horizontal interpolation (similar score values are obtained with SSDZ2001, HOR, HV and HN). This could be expected, given the widespread nature of this event (with smooth gradients of the reflectivity field in the horizontal –this can also be seen in the cross section of Fig. 3). Consequently, the scatter plots between rainfall accumulations produced from the reference and the reconstructed reflectivity with these methods show a very good agreement (as can be seen in

Fig. 4 for HOR). On the other hand, the performance of VERT is affected by the strong variability of reflectivity in the vertical (see Fig 3 top). As a result, the accumulated rain is systematically overestimated where the reconstruction uses PPIs affected by the bright band, and underestimated where the reconstruction uses observations extrapolated from the snow levels (see Fig. 4, middle panel). The use of previous quality-controlled volume scans (included in NOW, HN and HVN) results in relatively good reconstructions of the accumulated values (with correlation values above 0.96, Table 2). However, the information from previous time steps does not contribute to improve the reconstruction: the scores obtained with HOR and HV are, respectively, as good or better than those obtained with HN and HVN.

4.1.2 Convective case: 02 September 2004

This event was a convective situation that lasted for around 18 hours with several convective cells affecting mostly the coastal area and over the sea. Some of these cells had an important vertical development (up to 14 km, see the bottom cross section of Fig. 3) and lasted for a few hours.

In this case, reconstruction by horizontal interpolation (HOR) produced rather poor results (the correlation value is 0.75, bottom part of Table 2). Instead, reconstruction by vertical extrapolation (VERT) produces better results. In particular, Fig. 5 shows that VERT is able to better reproduce the high accumulation values than HOR. The combination of these two formulations (HV) benefits from the adaptive use of vertical and horizontal interpolation at each location and time, resulting in better scores (Table 2). Interestingly, the best reconstructions of the total accumulation for this event were obtained with the formulations using the previous quality-controlled volume scans (specially NOW and HVN). As shown in Fig. 5, NOW shows smaller biases and better reproduction of large rainfall accumulations.

The nature of this situation (the largest convective cell in front of the coast in the southern part of the domain was rather stationary and lasted for about 4 hours) particularly favored the use of time information. Contrarily, for other kinds of convective events (e.g., situations with small fast-evolving convective cells with short life times), one would not expect such a good performance with NOW.

4.1.3 Evaluation over 24 events

To provide a more robust evaluation of the proposed reconstruction method, 24 events (between 2001 and 2005) were chosen. The analyzed cases (summarized in Table 1) include a wide variety of rainfall situations. Figure 6 shows the bias, mean absolute relative error (MARE), the Pearson correlation coefficient and the root mean square error (RMSE) obtained for the total rainfall accumulations estimated using the different formulations to reconstruct reflectivity in the violet areas of Fig. 1. In general, the formulations that use multiple sources of information (SSDZ2001, HV, HN, and HVN) outperform those using a single source of information (HOR, VER, and NOW). Similarly as shown before, VERT has difficulties in reconstructing the accumulations for the widespread cases (as it is clear, for example, in the correlation panel of Fig. 6). The use of previous volume scans alone (NOW) is systematically not as good as the use of horizontal information alone (HOR) except for event #21 (the one presented in section 4.1.2). The adaptive combined use of horizontal and vertical interpolation (HV and HVN) results in consistently better reconstructions than SSDZ2001, which is based on either using horizontal interpolation or vertical extrapolation based on the identified precipitation type. Between HV and HVN, the latter seems to be less robust in a few cases (e.g., events #3, #5, #19, and #20), which shows that the contribution of time information can be sometimes counterproductive in combination with horizontal and vertical information.

4.2 Radar-raingauge comparison

The comparison between raingauge records and radar rainfall estimates is done in terms of event-accumulated rainfall (G and R, respectively). Radar rainfall accumulations are obtained from the first PPI (0.5º) of the reconstructed volume scans using a uniform Marshall and Palmer (1948) Z-R relation and accounting for the motion of the precipitation field and for the evolution of rainfall intensities within consecutive reflectivity scans [as discussed by Fabry et al. (1994)]. Radar estimates in areas where reflectivity measurements are affected by ground clutter in mean propagation conditions have been obtained with the different reconstruction methods (the location of raingauges in clutter-contaminated areas can be seen in Fig. 1). We have identified these R-G pairs as light grey squares in the R-G scatterplots (see e.g., Fig. 7). Consequently, a good reconstruction of the reflectivity values in these areas would make the squares fall within the cloud of R-G pairs shown as black dots (for raingauge locations where radar measurements are not affected by ground clutter). This would indicate that the reconstructed R values behave similarly as those in clutter-free areas. Other than this, we cannot expect the reconstruction methods to improve the R-G scatterplots, because the differences between raingauge observations and radar estimates are explained by a number of other factors (out of the scope of this paper) such as radar calibration errors, radome and path attenuation, the effect of not considering the vertical profile of reflectivity, the variability of the *Z–R* relationship, representativeness differences between radar and raingauges, or gauge problems.

On the other hand, we have analyzed the impact of the reconstruction techniques on (a) the conditional probability of 10-minute radar accumulations to exceed 0.1 mm given that the collocated raingauge measures rainfall ($P(Z \geq 0.1 \text{ mm} \mid R \geq 0.1 \text{ mm})$, i.e., the probability of rainfall detection, POD), and (b) the conditional probability of the radar estimating some

274 rainfall when raingauges measure no rainfall ($P(Z > 0.1 \text{ mm} \mid R = 0 \text{ mm})$, i.e., the probability
275 of false detection, POFD). Similarly to Berenguer et al. (2006), we have plotted the
276 dependence of these scores as a function of range. In general, the POD tends to decrease with
277 range due to the effect of beam overshooting in shallow precipitation, path attenuation, and
278 the fact that the radar sampling volume becomes bigger with range.

279 4.2.1 Widespread case: 11 May 2004

280 Figure 7 shows the scatter plots between collocated radar and raingauge accumulations
281 corresponding to this widespread case. The large scatter between radar and raingauge
282 accumulations at those locations where radar observations are not affected by ground clutter
283 (black dots in Fig. 7) can be in part explained by the effect of the vertical profile of
284 reflectivity (the bright band peak was around 1.9 km and affecting the first PPI between 60
285 and 90 km, Figs. 2 and 3).

286 Similarly as shown in Section 4.1.1, the use of the reflectivity measurements from PPIs aloft
287 to reconstruct clutter-contaminated reflectivity measurements in the first PPI (VERT) results
288 in increased scatter compared to HOR and NOW (for the latter two, the grey squares fall
289 within the cloud of black dots). Similar behavior is obtained with the formulations that
290 include horizontal interpolation (SSDZ2001, HV, HN, and HVN), which results in the scores
291 summarized in Table 3 (top).

292 The values of POD for HOR, NOW, and VERT (Fig. 8 left) are very close to 1.0 at near range
293 while those of POFD (Fig. 8 right) are around 0.2. However, VERT systematically
294 underdetects the occurrence of precipitation observed at ranges beyond 70 km (at these ranges
295 both the POD and the POFD for the grey squares are systematically lower than for the black
296 dots), due to the fact that the reconstruction uses observations extrapolated from the snow
297 region and even above precipitation. It is also worth highlighting the poor POD values at two

298 raingauge locations by NOW. These two raingauges are located in the middle of a large
299 ground clutter area on the north part of the domain, where the radar is scanning in the snow
300 layers (more prone to underdetection), and where the apparent motion is slow. These factors
301 result in that the reconstructed values are obtained by extrapolation from points where NOW
302 was already applied in the previous quality-controlled scan. Because of this, NOW uses data
303 extrapolated from around the clutter area that were actually recorded several time steps
304 before. As expected for a widespread case, the POD and POFD graphs for HV, HN, HVN and
305 SSDZ2001 (not shown) are very similar to those shown for HOR (Fig. 8 top).

306 4.2.2 Convective case: 02 September 2004

307 The scatter plots between radar estimates and raingauges observations are presented in Fig. 9.
308 In general, the radar-raingauge comparisons at the clutter-free locations (black dots) agree
309 well. For the reconstructed locations (light grey squares), HOR systematically underestimates
310 raingauge accumulations and performs worse than VERT and NOW (consistently with the
311 results seen in Section 4.1.2). The dependence of POD with range (Fig. 10) shows more
312 variability than that for the widespread event and is not clearly affected by the poor
313 performance of HOR. Instead, it produces a larger number of false detections (higher POFD).

314 On the other hand, the radar-raingauge plots for VERT and NOW are very similar and show
315 less biased accumulations than HOR (Fig. 9). However, in terms of the POD and POFD (Fig.
316 10), the reconstruction obtained with NOW is clearly worse than VERT within the first 50
317 km: The bottom panels of Fig. 10 show that in these ranges, NOW underdetected rain and
318 produced too many false detections (for some raingauges, POFD is over 0.4). We attribute
319 this result to the fast evolution of the rainfall systems near the radar (including initiation and
320 dissipation of small convective cells), which is not accounted for by the extrapolation of the
321 rainfall from the previous time step. This factor affects the POD and POFD, where the

322 analysis is done in terms of 10-minutes accumulations, while it has a less important effect in
323 terms of total event accumulations (as shown in Figs. 5 and 9) because misses and false
324 detections seem to compensate.

325 The bottom part of Table 3 shows similar scores among the formulations that combine
326 horizontal interpolation and vertical extrapolation (SSDZ2001, HV, and HVN), as a result of
327 the flexibility of these formulations to weigh the most representative observations in each
328 location and at each time step and confirming the results presented in section 4.1.2. The
329 results in terms of POD for these formulations (not shown) are slightly better than VERT in
330 terms, but this compensates with slightly worse performance in terms of POFD (in any case,
331 still clearly better than the results obtained with HOR or NOW).

332 #### 4.2.3 Evaluation over 24 events

333 Figure 11 summarizes the comparison between radar estimates and raingauges accumulations
334 in terms of bias, MARE, correlation and RMSE for the 24 analyzed events and for all the
335 formulations (similar as Fig. 6 for the analysis of the reconstruction over clutter-free areas).

336 The graphs show that for some events VERT and NOW clearly perform worse than the rest,
337 and, to a lesser extent, the same happens with HOR (for instance in event #5). Besides this,
338 very similar scores are obtained for most of the methods that combine different sources of
339 information. However, this does not necessarily imply that the different methods perform
340 similarly. As we have pointed out at the beginning of section 4.2, the interpretation of R-G
341 scores is not straightforward and needs to be done considering (i) that the scores have been
342 computed using all raingauges (in both clutter-free and clutter-affected areas) which in
343 general reduces the differences between methods, and (ii) the effect of the error sources in
344 radar QPE that have not been accounted in this study, which requires analyzing the results
345 event by event (similarly as done in Sections 4.2.1 and 4.2.2). These analyses (not shown

here) confirm the results presented for the two cases above and in Section 4.1.3: the combined use of horizontal and vertical information results in improved reconstructed accumulations, while the contribution of the information from the previous volume scan is not found significant.

5 Conclusion

In this study we have proposed and tested 6 different formulations of a method to reconstruct radar reflectivity in the areas affected by ground clutter. The proposed formulations interpolate clutter-free observations within the first PPI (horizontal interpolation), from the PPIs above (extrapolation in the vertical), and/or from the previous volume scan (extrapolation in time using a nowcasting technique). The interpolation is done in the Ordinary Kriging framework, which is based on the structural analysis of the field (in space and time) to determine the weights to be given to the available clutter-free observations. The structure of the field is characterized through the multi-dimensional sample semivariogram, which is estimated within the vicinity of each area to be reconstructed.

The evaluation of the proposed techniques has been done over 24 rainfall events in the area of Barcelona (NE of Spain). The reconstruction methods have been first applied over a clutter-free area (mostly over the sea). This allowed us to use the original observations as reference. However, it is worth pointing out that systematic differences in the space-time structure of precipitation over the sea and land could slightly bias the validity of the results. The second part of the evaluation has been performed over the actually clutter-contaminated areas using raingauge observations as reference.

Our results show the strengths and weaknesses of horizontal and vertical information for the reconstruction of the reflectivity fields:

- Horizontal interpolation shows its best performance in widespread precipitation, while it fails at handling the high horizontal variability of convective situations;
- Vertical extrapolation is useful in situations with deep convection, but is not a good solution in widespread rain, due to the larger variability of the radar fields in the vertical: it results in overestimation when the first clutter-free PPI is affected by the bright band, or underestimation when it is in the snow level or above. It is worth pointing out that these systematic errors in stratiform rain could be partially mitigated by implementing a VPR correction when extrapolating observations in the vertical [see Wesson and Pegram (2004); Bellon et al. (2007) and references therein].

These results coincide with what has been reported by other authors [e.g., Sánchez-Diezma et al. (2001)].

We have also implemented a nowcasting technique (NOW) to reconstruct reflectivity fields by extrapolation of the previous quality-controlled volume scan. On average, this approach has been found to be systematically not as good as horizontal interpolation alone. This is in part due to the fact that sometimes NOW uses reflectivitiy estimates that were already reconstructed in the previous time step (because the original observations were affected by clutter contamination). This significantly affects the quality of the reconstruction over large clutter areas. Also, time extrapolation might result in misses and false detections in cases with fast-evolving small-scale convection.

The adaptive interpolation of horizontal and vertical observations (HV) consistently improves the reconstruction of the reflectivity field thanks to the weight assigned to the available observations through the structural analysis of the field. Overall, the benefit of including information from the previous volume scan (extrapolation in time) in the interpolation is not

systematically evident: HN is in general outperformed by HV, while the results obtained with HVN are usually very similar to those of HV.

In conclusion, among the analyzed formulations, our recommendation for the reconstruction of reflectivity volume scans is to use HV because it produced the most robust results (with no outliers) and is computationally cheaper than HVN. Wesson and Pegram (2006) proposed a method similar to HV, also based on a kriging approach. The main difference from HV is in the representation of the field variability. They first apply a pre-classification of the type of precipitation, and then they use average parametric and isotropic semi-variograms adapted to each precipitation type.

Finally, the proposed framework is not only useful for the reconstruction of reflectivity fields, but it might also be interesting for other radar variables. In particular, the reconstruction of polarimetric variables will be explored in a forthcoming paper.

Acknowledgements

The Spanish Meteorology Agency (AEMET) provided radar data, and the Meteorological Service of Catalonia (SMC) and the Catalan Water Agency (ACA) provided raingauge observations. This work has been done in the framework of the Project of the Spanish Ministry of Economy and Competitiveness ProFEWS (CGL2010-15892). The second author is partially supported with a grant of the Ramón y Cajal Program of the Spanish Ministry of Economy and Competitiveness (RYC2010-06521). This study was stimulated from an initial idea and further discussion with Isztar Zawadzki (McGill University).

412 **Appendix A Estimation of the semivariogram**

413 One of the key points of the proposed method is the estimation of the semivariogram. We
414 have chosen to estimate the sample semivariogram using equation (3) [similarly as Velasco-
415 Forero et al. (2009); Sempere-Torres et al. (2012)]. The main difference with respect to these
416 authors is that we have estimated the semivariogram locally within a neighborhood of each
417 clutter area to better depict the local variability of the field.

418 This means that the most complete formulation (HVN) needs an estimate of the 4-
419 dimensional semivariogram $\gamma(\Delta x,\Delta y,\Delta z,\Delta t)$ around each ground echo area, with the
420 maximum lag in height, Δz_{max}, being the distance between the first PPI and the closest clutter-
421 free PPI, and Δt=10 minutes (the temporal resolution of radar data).

422 Figures A1 and A2 show an example for the first PPI measured on 06 July 20:03 at 16:20
423 UTC. The top panels show the reflectivity measurements within a subdomain of the radar
424 coverage from which the sample multi-dimensional semivariograms were estimated (bottom
425 panels of Figs. A1 and A2). The obvious differences between the estimated semivariograms
426 are due to the local differences in the spatial variability of the reflectivity field, which justifies
427 the need of estimating the semivariogram locally to guarantee the optimal reconstruction of
428 the field.

429 Similarly, the other configurations based on the Ordinary Kriging approach (namely, HOR,
430 HV and HN) make use of the 2-D and 3-D semi-variogram.

431

References

Bellon, A., Lee, G., Kilambi, A., Zawadzki, I., 2007. Real-time comparisons of VPR-corrected daily rainfall estimates with a gauge mesonet. Journal of Applied Meteorology and Climatology, 46(6): 726-741.

Berenguer, M., Sempere-Torres, D., Corral, C., Sanchez-Diezma, R., 2006. A fuzzy logic technique for identifying nonprecipitating echoes in radar scans. Journal of Atmospheric and Oceanic Technology, 23(9): 1157-1180.

Berenguer, M., Sempere-Torres, D., Pegram, G.G.S., 2011. SBMcast - An ensemble nowcasting technique to assess the uncertainty in rainfall forecasts by Lagrangian extrapolation. Journal of Hydrology, 404: 226-240.

Corral, C., Velasco, D., Forcadell, D., Sempere-Torres, D., 2009. Advances in radar-based flood warning systems. The EHIMI system and the experience in the Besòs flash-flood pilot basin. In: Samuels, P., Huntington, S., Allsop, W., Harrop, J. (Eds.), Flood Risk Management: Research and Practice. Taylor & Francis, London, UK, pp. 1295-1303.

Delrieu, G., Creutin, J.D., Andrieu, H., 1995. Simulation of Radar Mountain Returns Using a Digitized Terrain Model. Journal of Atmospheric and Oceanic Technology, 12(5): 1038-1049.

Doviak, R.J., Zrnic, D.S., 1993. Doppler radar and weather observations, 562 pp.

Fabry, F., Bellon, A., Duncan, M.R., Austin, G.L., 1994. High-Resolution Rainfall Measurements by Radar for Very Small Basins - the Sampling Problem Reexamined. Journal of Hydrology, 161(1-4): 415-428.

454 Germann, U., Galli, G., Boscacci, M., Bolliger, M., 2006. Radar precipitation measurement in
455 a mountainous region. Quarterly Journal of the Royal Meteorological Society,
456 132(618): 1669-1692.

457 Goovaerts, P., 1997. Geostatistics for natural resources evaluation. Applied Geostatistics
458 Series. Oxford University Press, 483 pp.

459 Gourley, J.J., Tabary, P., Parent du Chatelet, J., 2007. A Fuzzy Logic Algorithm for the
460 Separation of Precipitating from Nonprecipitating Echoes Using Polarimetric Radar
461 Observations. Journal of Atmospheric and Oceanic Technology, 24(8): 1439-1451.

462 Hubbert, J.C., Dixon, M., Ellis, S.M., 2009. Weather Radar Ground Clutter. Part II: Real-
463 Time Identification and Filtering. Journal of Atmospheric and Oceanic Technology,
464 26(7): 1181.

465 Marshall, J.S., Palmer, W.M., 1948. The Distribution of Raindrops with Size. Journal of
466 Meteorology, 5(4): 165-166.

467 Moisseev, D.N., Chandrasekar, V., 2009. Polarimetric Spectral Filter for Adaptive Clutter and
468 Noise Suppression. Journal of Atmospheric and Oceanic Technology, 26(2): 215.

469 Sanchez-Diezma, R., Sempere-Torres, D., Creutin, J.-D., Zawadzki, I., Delrieu, G., 2001. An
470 improved methodology for ground clutter substitution based on a pre-classification of
471 precipitaion types, 30th International Conference on Radar Meteorology. Amer.
472 Meteor. Soc., Munich, Germany, pp. 271-273.

473 Sempere-Torres, D., Berenguer, M., Velasco-Forero, C.A., 2012. Blending of radar and gauge
474 rainfall measurements. A preliminary analysis of the impact of measurement errors,

475 Weather Radar and Hydrology (Proceedings of a symposium held in Exeter, UK,
476 April 2011). IAHS, pp. 365.

477 Sempere-Torres, D., Porra, J.M., Creutin, J.D., 1998. Experimental evidence of a general
478 description for raindrop size distribution properties. Journal of Geophysical Research-
479 Atmospheres, 103(D2): 1785-1797.

480 Steiner, M., Smith, J.A., 2002. Use of Three-Dimensional Reflectivity Structure for
481 Automated Detection and Removal of Nonprecipitating Echoes in Radar Data. Journal
482 of Atmospheric and Oceanic Technology, 19(5): 673-686.

483 Velasco-Forero, C.A., Sempere-Torres, D., Cassiraga, E.F., Gómez-Hernández, J.J., 2009. A
484 non-parametric automatic blending methodology to estimate rainfall fields from rain
485 gauge and radar data. Advances in Water Resources, 32(7): 986-1002.

486 Villarini, G., Krajewski, W.F., 2009. Review of the Different Sources of Uncertainty in
487 Single Polarization Radar-Based Estimates of Rainfall. Surveys in Geophysics, 31(1):
488 107-129.

489 Wesson, S.M., Pegram, G.G.S., 2004. Radar rainfall image repair techniques. Hydrol. Earth
490 Syst. Sci., 8(2): 220-234.

491 Wesson, S.M., Pegram, G.G.S., 2006. Improved radar rainfall estimation at ground level.
492 Natural Hazards and Earth System Sciences, 6: 323-342.

493 Zawadzki, I.I., 1973. Statistical Properties of Precipitation Patterns. Journal of Applied
494 Meteorology, 12(3): 459-472.

495

496 Table 1. Summary of the 24 events analyzed in this study. Types "C" and "S" stand for
497 "convective" and "stratiform", respectively. #gauges indicates the number of rain gauges that
498 measured significant rain during the event. Mean and Max stand for the average and
499 maximum rainfall observed or estimated at rain gauge locations. CV is the coefficient of
500 variation of rainfall accumulations at raingauge locations (defined as the ratio between the
501 standard deviation and the mean value; i.e., high CV values indicate significant spatial
502 variability of the accumulated field).

				Rain gauges				Radar		
	Event start	Duration [h]	Type	# gauges	Mean [mm]	Max [mm]	CV	Mean [mm]	Max [mm]	CV
#1	14/07/2001 01:00	23.0	C	49	12.5	71.3	1.27	7.8	44.1	1.30
#2	15/07/2001 00:00	13.0	C	76	21.3	65.0	0.63	18.8	59.9	0.61
#3	15/07/2001 17:00	28.0	C/S	57	12.6	43.4	0.86	11.6	39.5	0.73
#4	19/07/2001 00:00	20.0	S	101	23.1	38.6	0.35	22.5	40.4	0.37
#5	14/11/2001 00:00	96.0	S/C	105	65.9	167.1	0.38	55.3	209.0	0.52
#6	08/08/2002 00:00	20.0	C/S	88	7.0	36.8	0.91	6.2	27.6	0.78
#7	09/08/2002 12:00	12.0	S	80	6.2	34.6	1.01	3.8	15.5	0.75
#8	10/08/2002 05:00	16.0	C	62	10.6	47.3	0.82	9.1	37.7	0.96
#9	22/08/2002 00:00	21.0	S/C	86	16.5	60.1	0.82	12.8	38.1	0.54
#10	26/08/2002 00:00	24.0	C	66	14.6	71.9	1.08	9.5	51.1	1.03
#11	08/10/2002 18:00	54.0	C/S	107	73.4	193.3	0.46	61.3	152.1	0.31
#12	24/11/2002 00:00	24.0	S	106	24.1	47.8	0.34	23.4	60.2	0.42
#13	10/12/2002 00:00	24.0	S/C	101	43.7	96.5	0.52	28.4	90.5	0.66
#14	06/07/2003 01:00	20.0	C	36	8.4	34.4	1.01	8.4	35.1	0.91
#15	17/08/2003 03:00	21.0	C/S	100	22.3	64.2	0.56	15.3	50.1	0.49
#16	04/09/2003 05:00	40.0	S/C	65	8.7	38.4	1.04	9.4	60.4	1.32
#17	07/09/2003 01:00	18.0	S/C	96	18.0	56.3	0.65	9.8	27.4	0.43
#18	22/09/2003 00:00	24.0	C	77	12.2	68.4	1.03	10.6	72.1	0.96
#19	16/04/2004 00:00	24.0	S	100	43.3	142.8	0.78	25.5	60.6	0.47
#20	11/05/2004 00:00	24.0	S	104	12.8	21.6	0.28	9.9	19.2	0.41
#21	02/09/2004 00:00	18.0	C	76	10.1	73.3	1.25	9.8	43.7	0.90
#22	03/09/2004 00:00	12.0	C/S	95	15.0	37.7	0.60	11.3	21.9	0.31

#23	12/10/2005 00:00	51.0	S/C	104	61.8	259.4	0.62	51.5	242.7	0.59
#24	14/10/2005 07:00	41.0	S/C	102	31.4	78.0	0.43	26.6	49.7	0.36

503

504

505 Table 2. Scores obtained for the reconstruction of event accumulations in clutter-free areas
506 (analysis of section 4.1) with the different reconstruction methods for the examples of 11 May
507 2004 (Event #20 of Table 1) and 02 September2004 (Event #21 of Table 1). The light gray
508 shaded cells indicate the method for which the best score is obtained.

Widespread case: 11 May 2004 00:00 – 24:00

	SSDZ2001	HOR	VERT	NOW	HV	HN	HVN
Bias [mm]	0.07	0.12	-5.17	-0.37	0.08	-0.12	1.2
RMSE [mm]	0.49	0.54	7.86	0.91	0.53	0.57	1.71
MARE [%]	4.3	4.7	68.9	8.2	4.5	4.8	15.2
Correlation	0.99	0.99	0.20	0.97	0.99	0.99	0.96

Convective case: 02 Sep 2004 00:00 – 24:00

	SSDZ2001	HOR	VERT	NOW	HV	HN	HVN
Bias [mm]	-1.44	-0.51	-0.48	0.33	-0.42	-0.58	-0.26
RMSE [mm]	2.78	3.27	2.52	2.28	2.37	2.57	1.85
MARE [%]	57.0	96.3	89.0	45.5	73.5	78.7	59.6
Correlation	0.77	0.75	0.83	0.90	0.87	0.87	0.92

509

510 Table 3. Same as Table 2, but for the comparison of radar and raingauge totals (section 4.2).

Widespread case: 11 May 2004 00:00 – 24:00

	SSDZ2001	HOR	VERT	NOW	HV	HN	HVN
Bias [mm]	-2.89	-2.89	-2.88	-3.08	-2.89	-2.99	-2.45
RMSE [mm]	4.35	4.35	4.70	4.58	4.36	4.45	4.24
MARE [%]	35.9	35.9	38.8	37.9	36.0	36.6	35.3
Correlation	0.36	0.36	0.27	0.35	0.36	0.34	0.35

Convective case: 02 Sep 2004 00:00 – 24:00

	SSDZ2001	HOR	VERT	NOW	HV	HN	HVN
Bias [mm]	-0.60	-1.56	-0.99	-0.61	-1.03	-1.03	-0.80
RMSE [mm]	4.16	4.46	4.10	4.20	4.08	4.39	4.08
MARE [%]	66.1	65.8	61.1	68.4	62.2	69.1	63.0
Correlation	0.84	0.83	0.83	0.83	0.85	0.83	0.84

511

List of Figure captions

Figure 1. Area where the experiment has been carried out and mean ground clutter map in clear-air conditions for the domain covered by the Barcelona radar (the location of the radar is indicated by the white diamond). The violet shaded areas show where the signal has been reconstructed for the evaluation of the different formulations (analysis presented in section 4.1). The orange diamonds show the location of the raingauges used for the evaluation of the performance of the formulations (section 4.2).

Figure 2. Top: Reflectivity measurements on the first PPI observed on 11 May 2004 at 13:10 UCT (left) and on 02 September 2004 at 07:30 UTC (right). Bottom: Estimated rainfall accumulation during the two example cases of 11 May 2004 (left) and 02 September 2004 (right).

Figure 3. Vertical cross sections of the reflectivity volume scans shown in Fig 2 on 11 May 2014 at 13:10 UTC along the segment A-B (top) and 02 September 2004 at 07:30 UTC along the segment C-D (bottom). Radar beam paths for different elevations (thin green lines) have been calculated supposing normal propagation conditions. The black shades are the terrain profile along the cross sections.

Figure 4. Scatterplots between reference and reconstructed rainfall accumulations over the violet clutter-free areas shown in Fig. 1 for the event of 11 May 2004. The reconstruction has been performed over reflectivity volume scans with the HOR, VERT and NOW methods (left, middle, and right panels, respectively).

Figure 5. Same as Fig. 4, but for the event of 02 September 2004.

Figure 6. From top to bottom, accumulation bias, MARE, correlation, and RMSE over the clutter-free areas (shown in Fig. 1) where the 6 tested formulations and SSDZ2001 have been

used to reconstruct the reflectivity (section 4.1). The results are presented for the 24 analyzed events (note that, despite of the use of lines, the events are in no way connected).

Figure 7. Scatterplots of accumulated raingauge rainfall and radar estimates for a widespread rain event (11 May 2004, #20 of Table 1). Reconstruction of radar reflectivity in clutter-contaminated areas has been done with HOR (left), VERT (middle), and NOW (right). Light gray squares correspond to rain gauges collocated with radar bins affected by clutter in mean propagation conditions. Black dots correspond to rain gauges in areas not affected by clutter.

Figure 8. POD (left) and POFD (right) as a function of range corresponding to a widespread case (11 May 2004, #20 of Table 1). The reconstruction of radar reflectivity in clutter-contaminated areas has been done (from top to bottom) with HOR, VERT and NOW. Light gray squares correspond to rain gauges collocated with radar bins affected by clutter in mean propagation conditions. Black dots correspond to rain gauges in areas not affected by clutter.

Figure 9. Same as Fig. 7, but for a convective case (02 September 2004, #21 of Table 1).

Figure 10. Same as Fig. 8, but for a convective case (02 September 2004, #21 of Table 1)

Figure 11. Similar as Fig. 6, but for the radar-raingauge comparison (section 4.2)

Figure A1. Top: Subdomain (northeast of the radar) of the reflectivity field observed on 06 July 2003 at 16:20 UTC on the first PPI (left), on the second PPI (middle) and, on the first PPI observed from 16:10 UTC extrapolated to compensate the effect of motion (right). The areas in white are affected by ground clutter, and thus have not been used to estimate the semivariogram. Bottom: 2D semivariogram estimated within the subdomain (expressed in units of % of the field variance) for lags, $\Delta z=0$ and $\Delta t=0$ (left), $\Delta z=1$ PPI and $\Delta t=0$ (middle), and $\Delta z=0$ and $\Delta t=10$ minutes (right).

557 Figure A2. Same as Fig. A1, but for another subdomain (northwest of the radar).

Figure 1

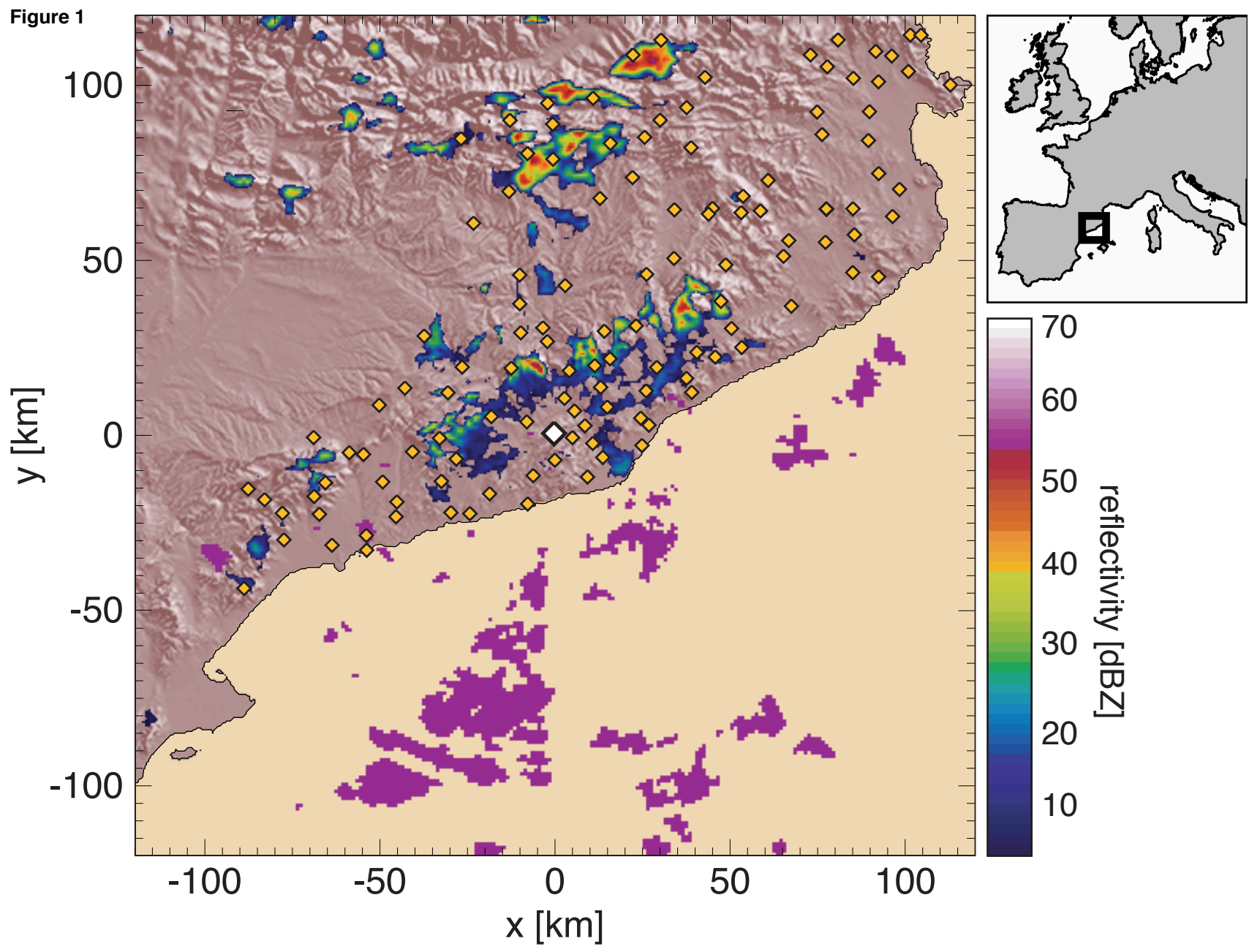
100
50
0
-50
-100
y [km]
-100
-50
0
50
100
x [km]
70
60
50
40
30
20
10
reflectivity [dBZ]

Figure 2

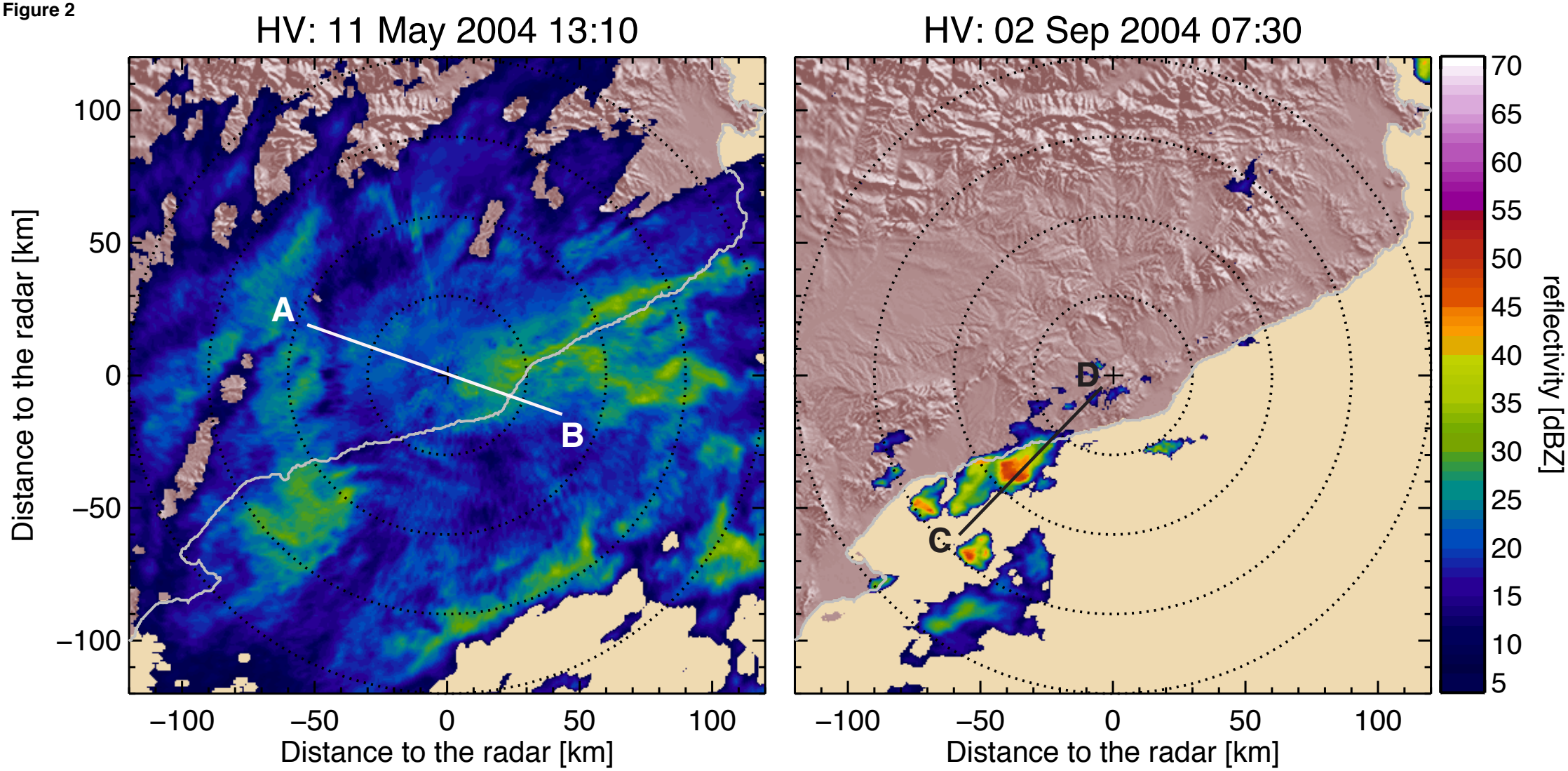
HV: 11 May 2004 13:10
HV: 02 Sep 2004 07:30
A
B
C
D
Distance to the radar [km]
Distance to the radar [km]
reflectivity [dBZ]
70
65
60
55
50
45
40
35
30
25
20
15
10
5
100
50
0
−50
−100
−100
−50
0
50
100

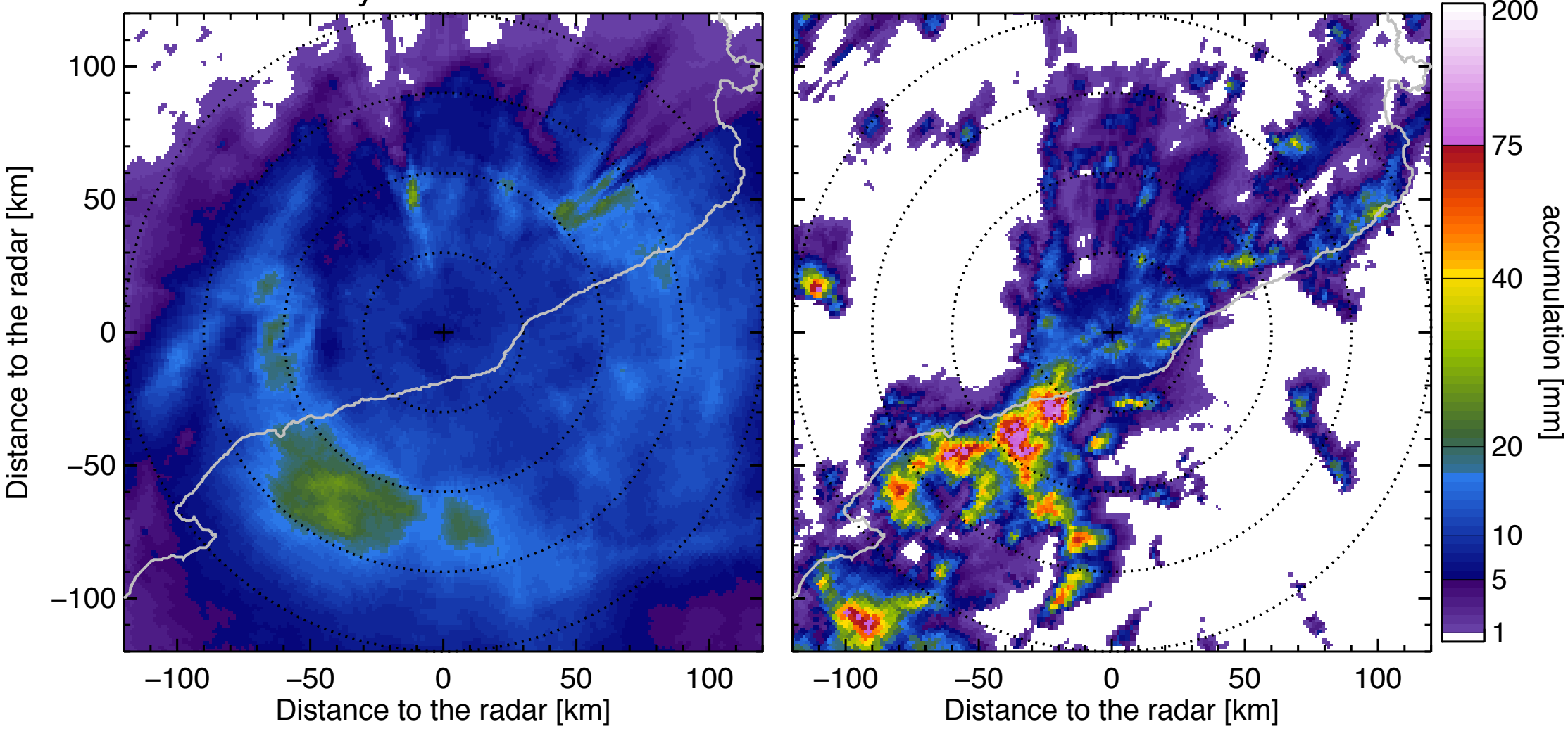
HV: 11 May 2004 00:00 – 24:00
HV 02/09/2004 00:00 – 18:00
Distance to the radar [km]
Distance to the radar [km]
accumulation [mm]
200
75
40
20
10
5
1
100
50
0
−50
−100
−100
−50
0
50
100

Figure 3

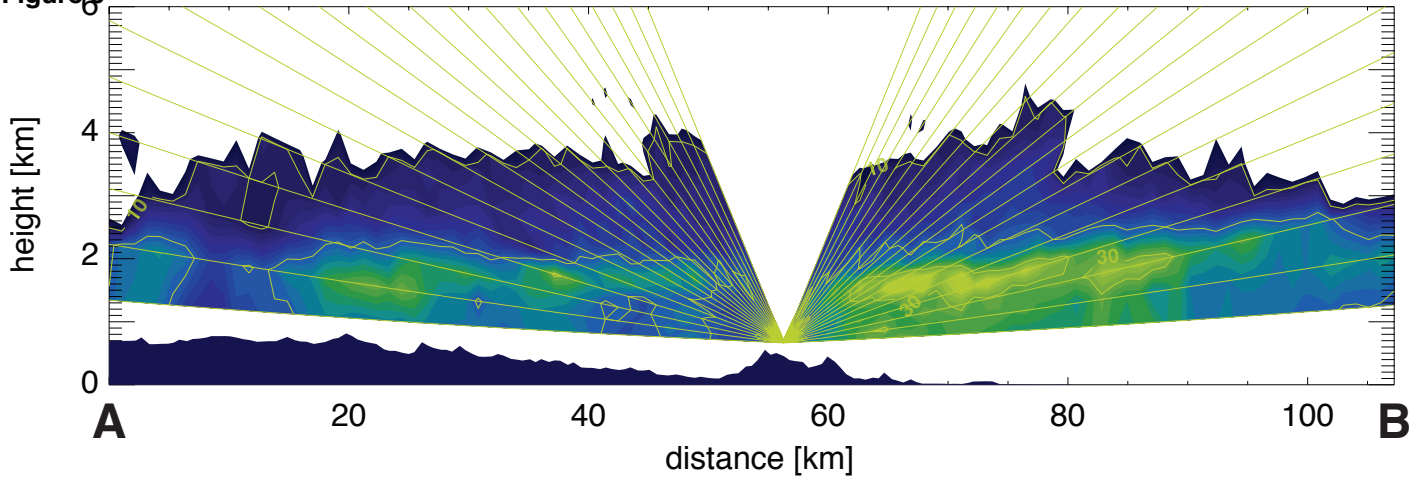
height [km]
0
2
4
6
A
20
40
60
80
100
B
distance [km]
10
30

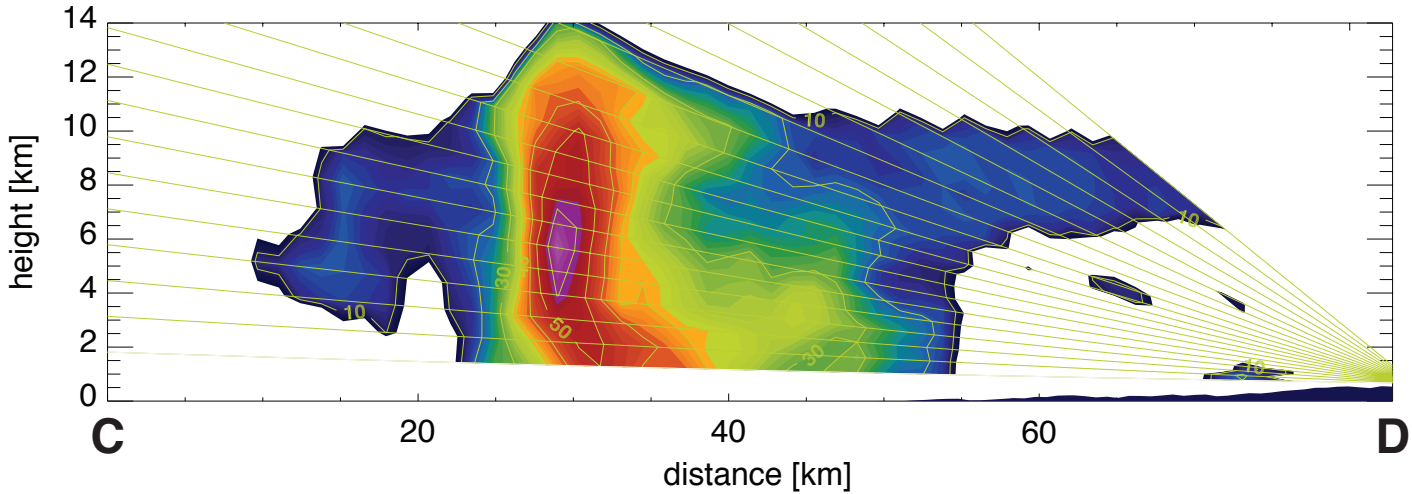
height [km]
0
2
4
6
8
10
12
14
C
20
40
60
D
distance [km]
10
30
50

Figure 4

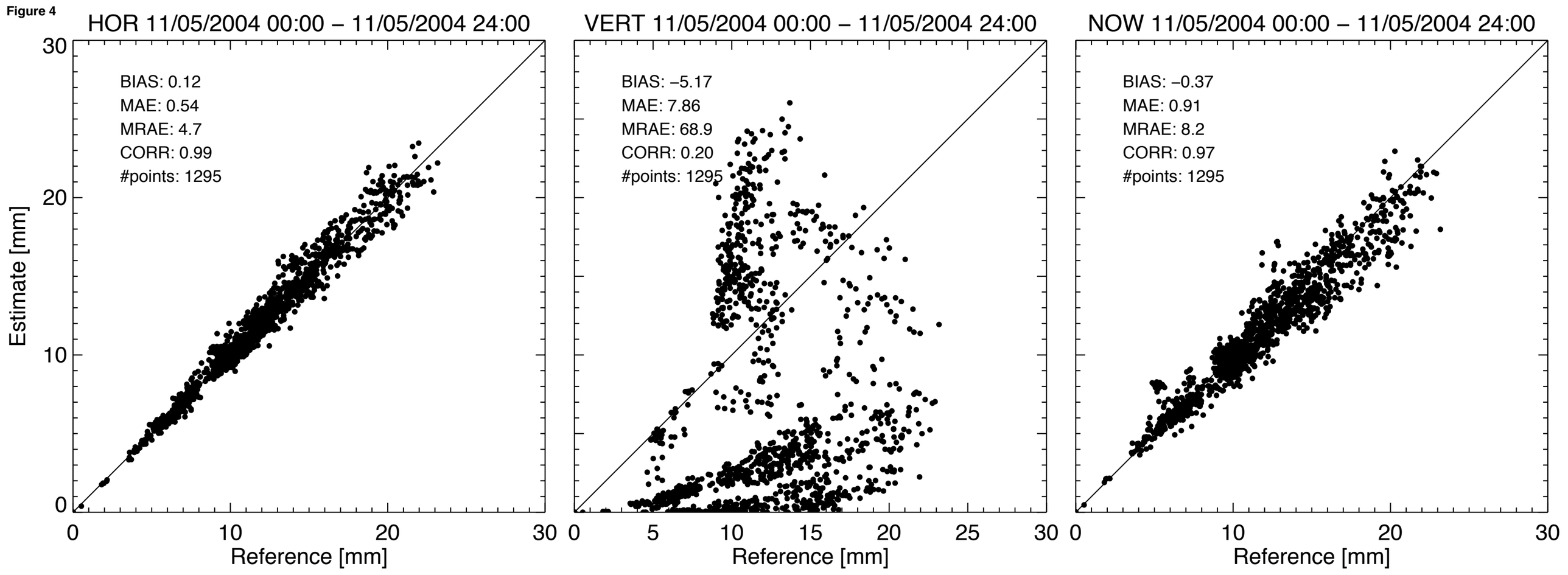
HOR 11/05/2004 00:00 – 11/05/2004 24:00
BIAS: 0.12
MAE: 0.54
MRAE: 4.7
CORR: 0.99
#points: 1295
VERT 11/05/2004 00:00 – 11/05/2004 24:00
BIAS: –5.17
MAE: 7.86
MRAE: 68.9
CORR: 0.20
#points: 1295
NOW 11/05/2004 00:00 – 11/05/2004 24:00
BIAS: –0.37
MAE: 0.91
MRAE: 8.2
CORR: 0.97
#points: 1295
Estimate [mm]
Reference [mm]
Reference [mm]
Reference [mm]

Figure 5

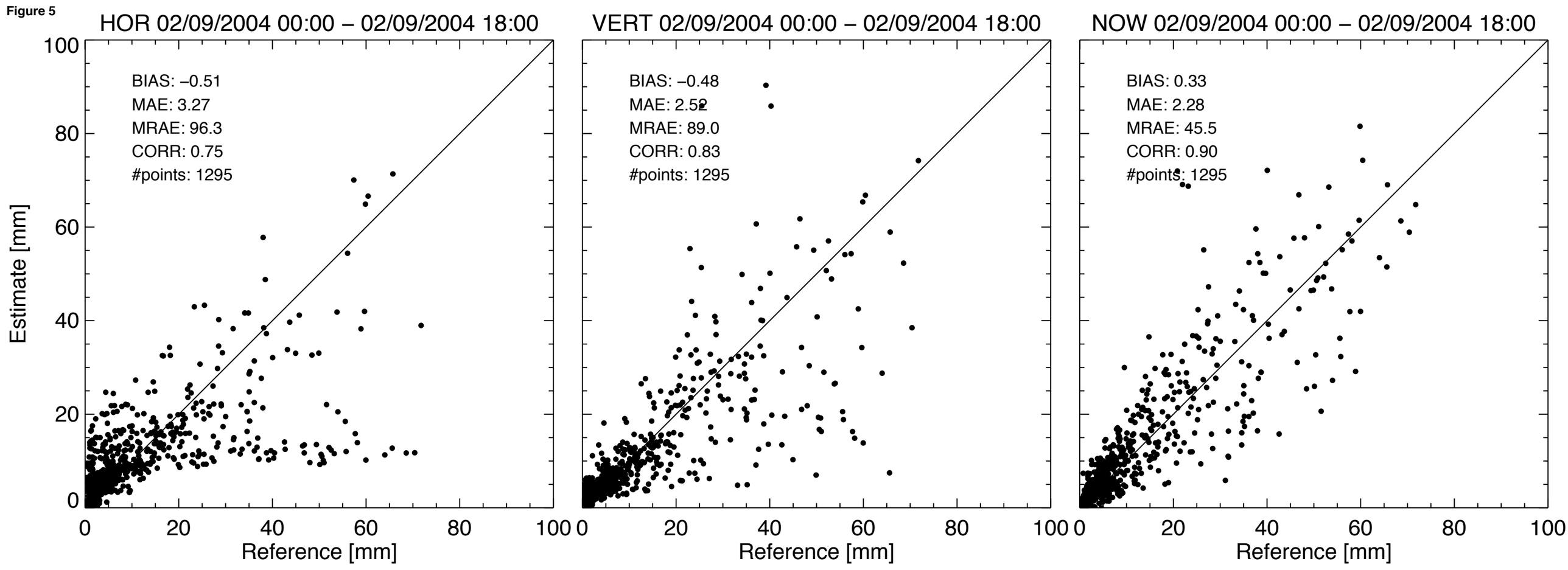
HOR 02/09/2004 00:00 – 02/09/2004 18:00
BIAS: –0.51
MAE: 3.27
MRAE: 96.3
CORR: 0.75
#points: 1295
VERT 02/09/2004 00:00 – 02/09/2004 18:00
BIAS: –0.48
MAE: 2.52
MRAE: 89.0
CORR: 0.83
#points: 1295
NOW 02/09/2004 00:00 – 02/09/2004 18:00
BIAS: 0.33
MAE: 2.28
MRAE: 45.5
CORR: 0.90
#points: 1295
Estimate [mm]
Reference [mm]
Reference [mm]
Reference [mm]
0
20
40
60
80
100

Figure 6

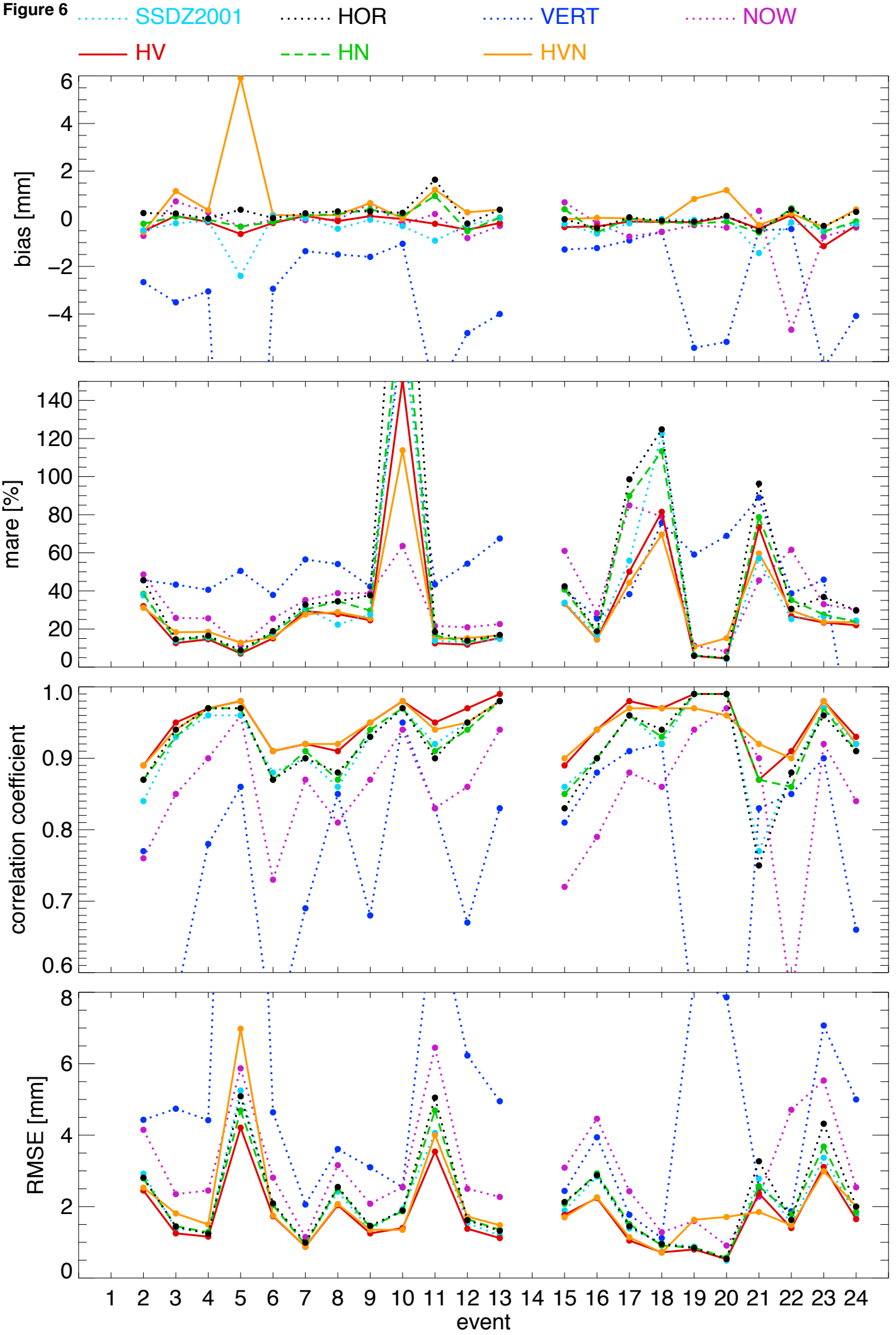
SSDZ2001
HOR
VERT
NOW
HV
HN
HVN
bias [mm]
mare [%]
correlation coefficient
RMSE [mm]
event

Figure 7

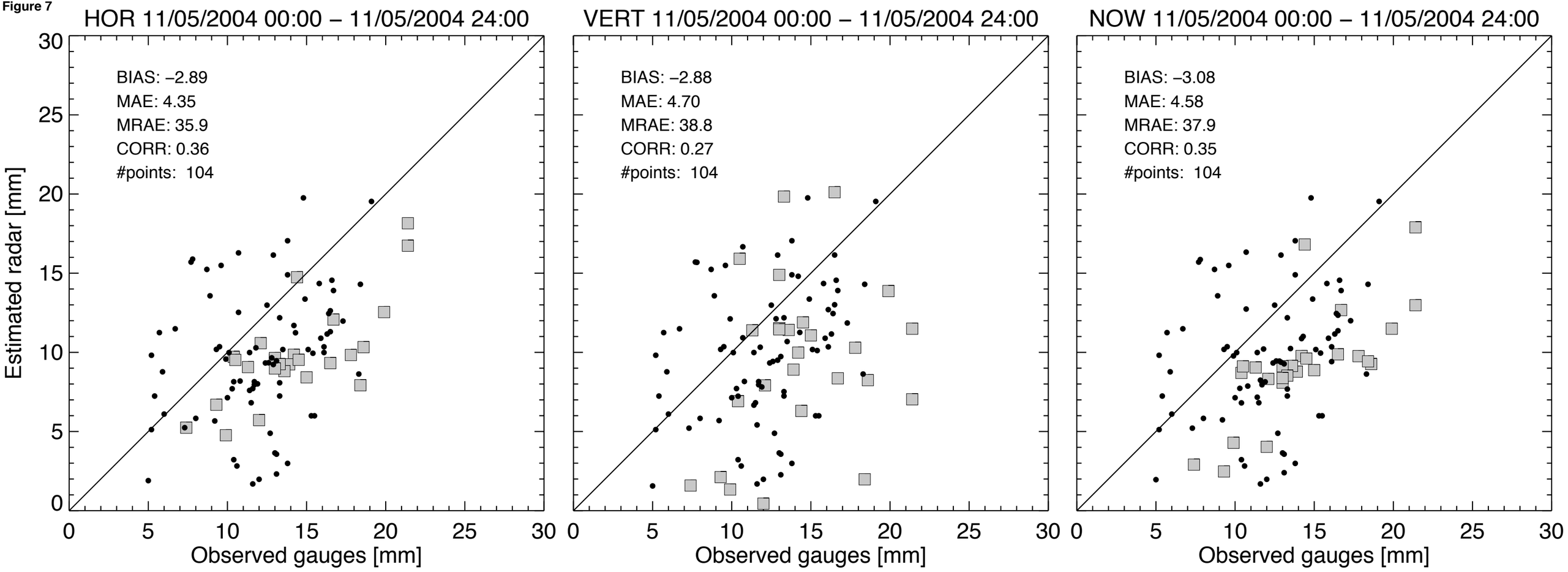
HOR 11/05/2004 00:00 – 11/05/2004 24:00
BIAS: –2.89
MAE: 4.35
MRAE: 35.9
CORR: 0.36
#points: 104
VERT 11/05/2004 00:00 – 11/05/2004 24:00
BIAS: –2.88
MAE: 4.70
MRAE: 38.8
CORR: 0.27
#points: 104
NOW 11/05/2004 00:00 – 11/05/2004 24:00
BIAS: –3.08
MAE: 4.58
MRAE: 37.9
CORR: 0.35
#points: 104
Estimated radar [mm]
Observed gauges [mm]
Observed gauges [mm]
Observed gauges [mm]
0
5
10
15
20
25
30

Figure 8

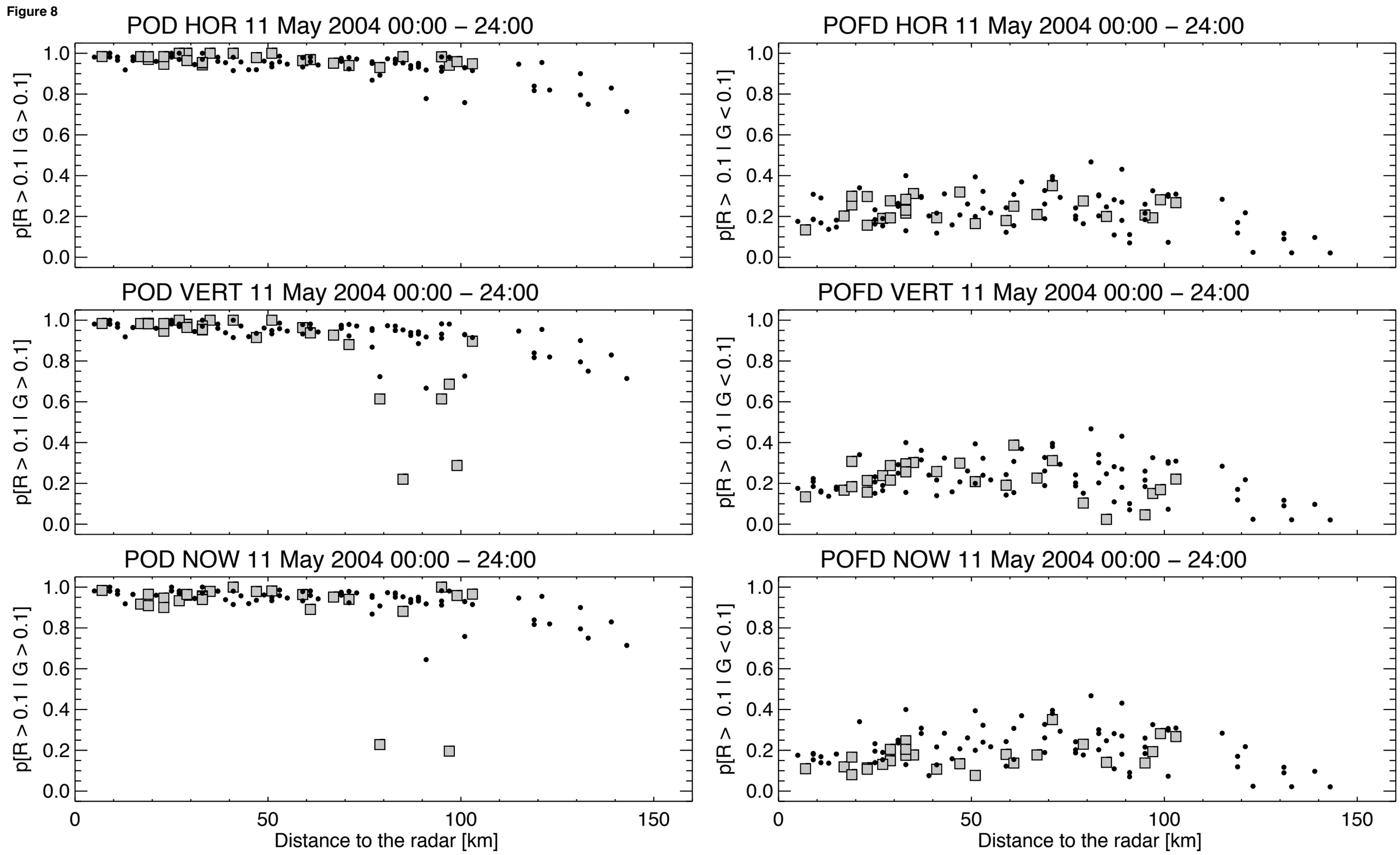
POD HOR 11 May 2004 00:00 – 24:00
POFD HOR 11 May 2004 00:00 – 24:00
POD VERT 11 May 2004 00:00 – 24:00
POFD VERT 11 May 2004 00:00 – 24:00
POD NOW 11 May 2004 00:00 – 24:00
POFD NOW 11 May 2004 00:00 – 24:00
p[R > 0.1 I G > 0.1]
p[R > 0.1 I G < 0.1]
0.0
0.2
0.4
0.6
0.8
1.0
0
50
100
150
Distance to the radar [km]

Figure 9

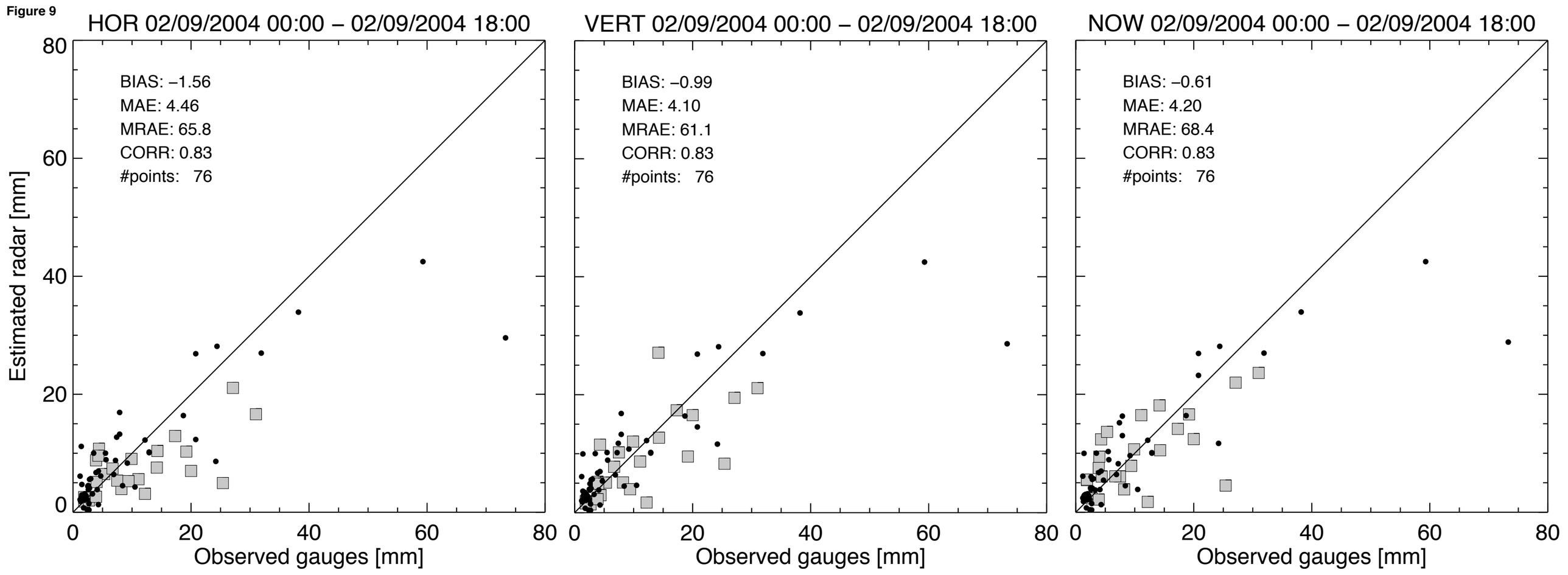
HOR 02/09/2004 00:00 – 02/09/2004 18:00
BIAS: –1.56
MAE: 4.46
MRAE: 65.8
CORR: 0.83
#points: 76
VERT 02/09/2004 00:00 – 02/09/2004 18:00
BIAS: –0.99
MAE: 4.10
MRAE: 61.1
CORR: 0.83
#points: 76
NOW 02/09/2004 00:00 – 02/09/2004 18:00
BIAS: –0.61
MAE: 4.20
MRAE: 68.4
CORR: 0.83
#points: 76
Estimated radar [mm]
Observed gauges [mm]
0
20
40
60
80

Figure 10

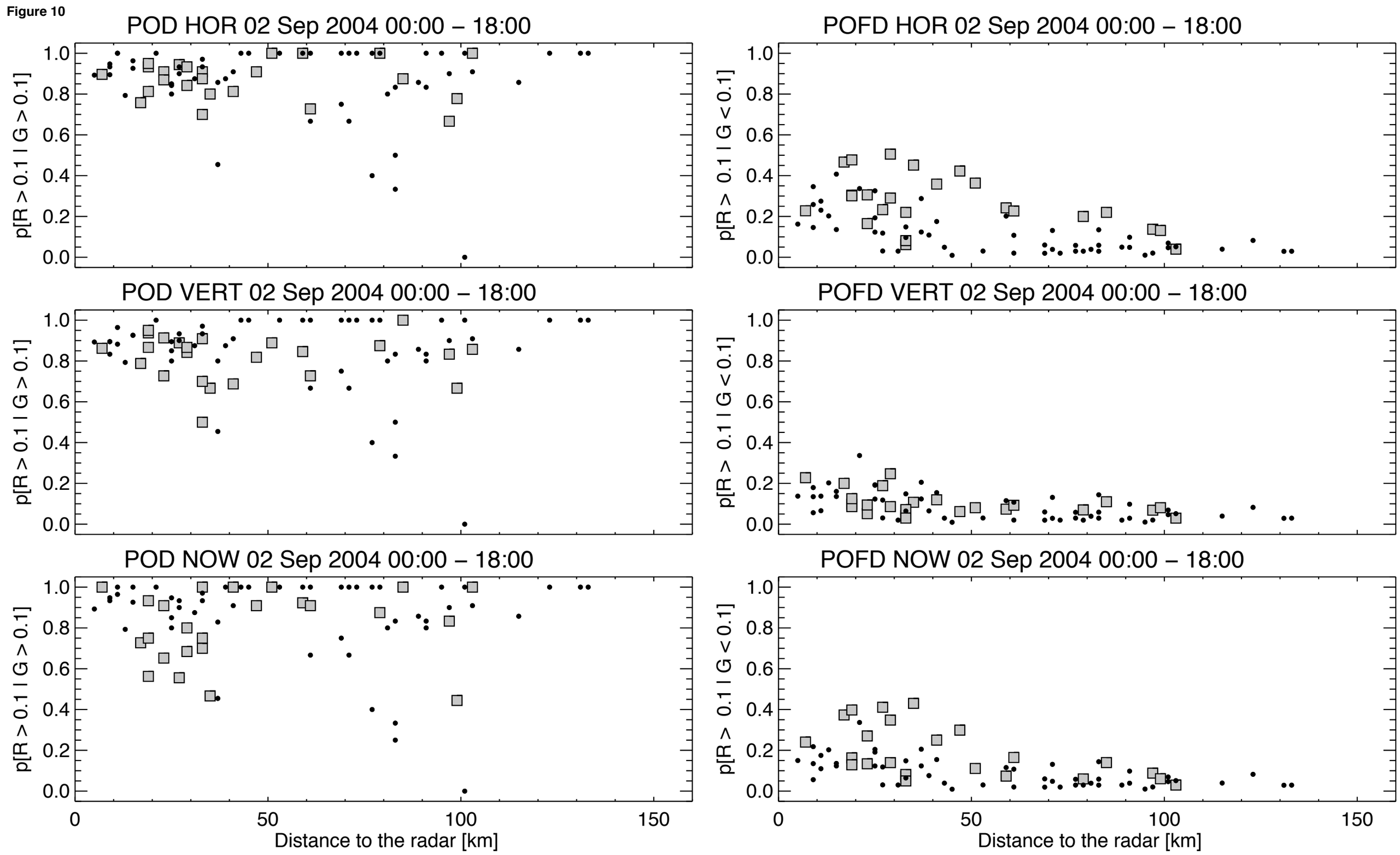
POD HOR 02 Sep 2004 00:00 – 18:00
POFD HOR 02 Sep 2004 00:00 – 18:00
POD VERT 02 Sep 2004 00:00 – 18:00
POFD VERT 02 Sep 2004 00:00 – 18:00
POD NOW 02 Sep 2004 00:00 – 18:00
POFD NOW 02 Sep 2004 00:00 – 18:00
p[R > 0.1 I G > 0.1]
p[R > 0.1 I G < 0.1]
0.0
0.2
0.4
0.6
0.8
1.0
0
50
100
150
Distance to the radar [km]

Figure 11

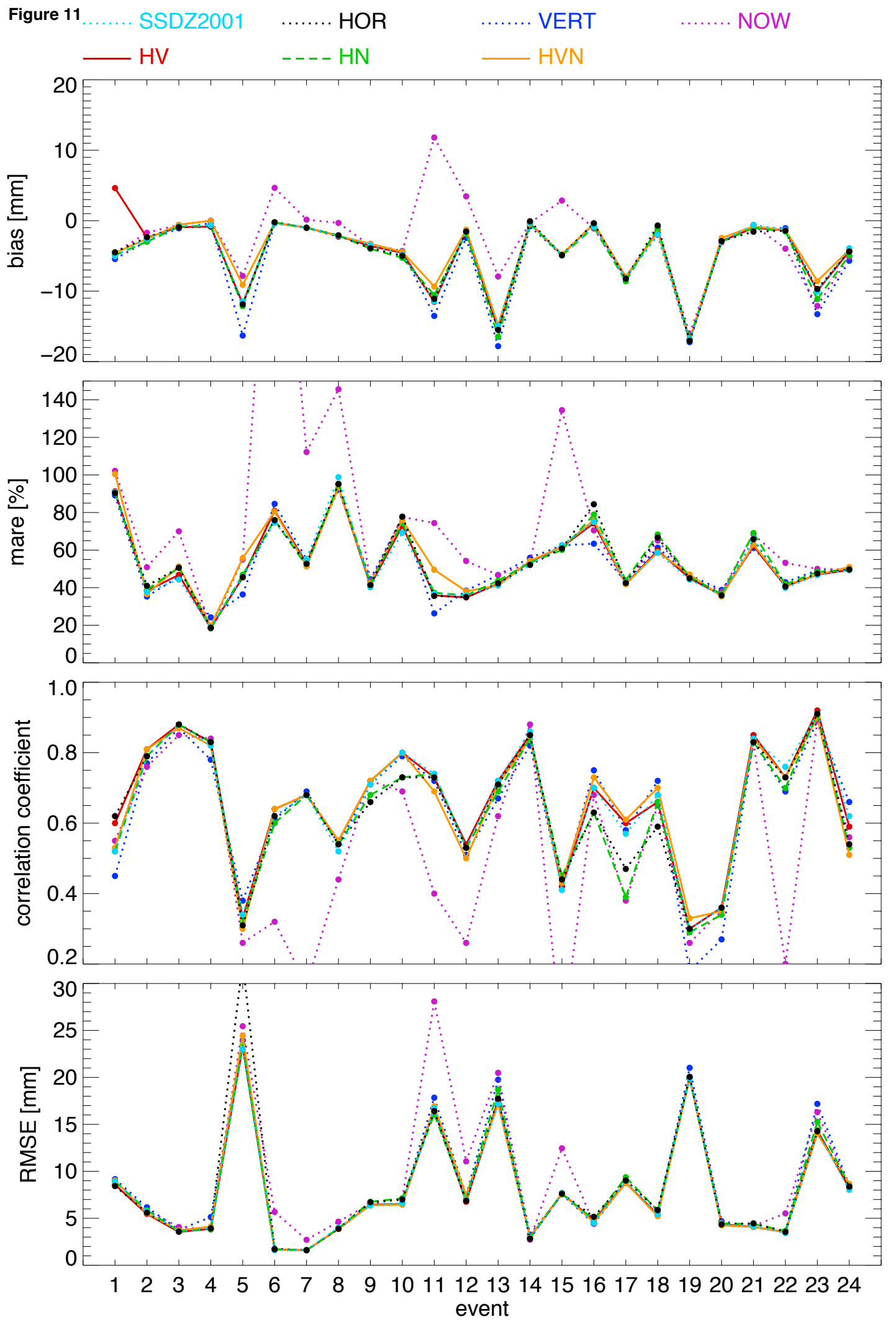
SSDZ2001
HOR
VERT
NOW
HV
HN
HVN
bias [mm]
mare [%]
correlation coefficient
RMSE [mm]
event

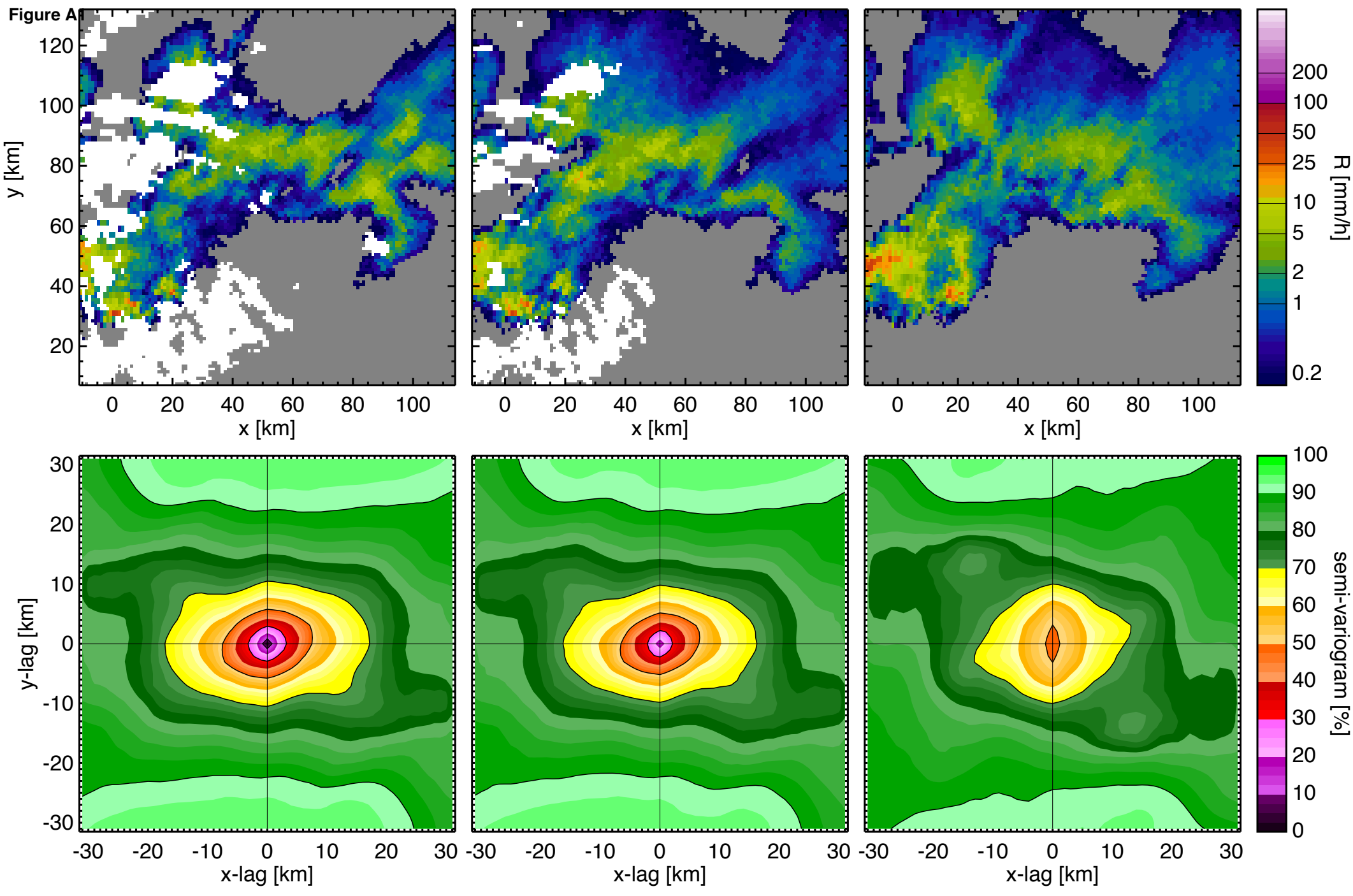
Figure A
y [km]
x [km]
R [mm/h]
200
100
50
25
10
5
2
1
0.2
y-lag [km]
x-lag [km]
semi-variogram [%]
100
90
80
70
60
50
40
30
20
10
0

Figure A2

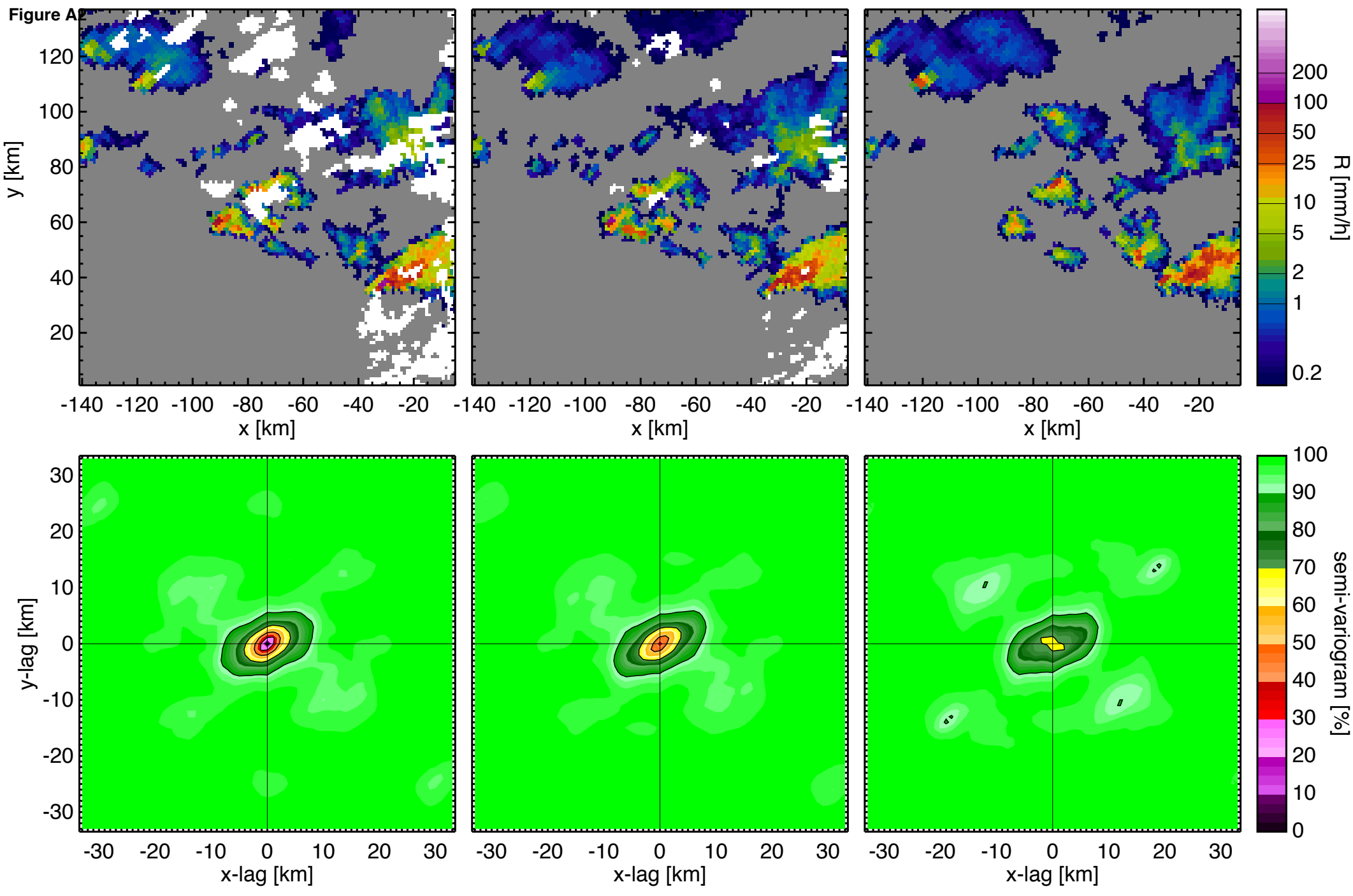
y [km]
120
100
80
60
40
20
-140 -120 -100 -80 -60 -40 -20
x [km]
R [mm/h]
200
100
50
25
10
5
2
1
0.2
y-lag [km]
30
20
10
0
-10
-20
-30
-30 -20 -10 0 10 20 30
x-lag [km]
semi-variogram [%]
100
90
80
70
60
50
40
30
20
10
0